Evidence for a $J_{\mathrm{eff}} = 0$ ground state and defect-induced spin glass behavior in the pyrochlore osmate Y$_2$Os$_2$O$_7$

N. R. Davies,[1] C. V. Topping,[1] H. Jacobsen,[1] A. J. Princep,[1] F. K. K. Kirschner,[1] M. C. Rahn,[1,*] M. Bristow,[1]
J. G. Vale,[2] I. da Silva,[3] P. J. Baker,[3] Ch. J. Sahle,[4] Y.-F. Guo,[5] D.-Y. Yan,[6] Y.-G. Shi,[6] S. J. Blundell,[1]
D. F. McMorrow,[2] and A. T. Boothroyd[1,†]

[1]*Department of Physics, University of Oxford, Clarendon Laboratory, Oxford OX1 3PU, United Kingdom*
[2]*London Centre for Nanotechnology and Department of Physics and Astronomy, University College London,*
Gower Street, London WC1E 6BT, United Kingdom
[3]*ISIS Facility, STFC Rutherford Appleton Laboratory, Harwell Campus, Didcot OX11 0QX, United Kingdom*
[4]*European Synchrotron Radiation Facility, 71 Avenue des Martyrs, 38000 Grenoble, France*
[5]*School of Physical Science and Technology, ShanghaiTech University, 319 Yueyang Road, Shanghai 200031, China*
[6]*Beijing National Laboratory for Condensed Matter Physics & Institute of Physics, Chinese Academy of Science, Beijing 100190, China*

We present AC and DC magnetometry, heat capacity, muon spin relaxation (μSR), and resonant inelastic x-ray scattering (RIXS) studies of the pyrochlore osmate Y$_2$Os$_2$O$_7$. Consistent with previous results, we observe a small Curie-Weiss effective moment of approximately 0.4 μ_{B} and spin freezing at a temperature $T_f \simeq 5$ K. On the other hand, our analysis of the RIXS spectra with single-ion energy-level calculations implies a nonmagnetic $J_{\mathrm{eff}} = 0$ ground state on the Os^{4+} sites, with the spin-orbit interaction, Hund's coupling, and trigonal distortion of OsO$_6$ octahedra, all important in modeling the observed spectra. From high-field magnetization data, we show that the paramagnetic moment is most likely due to large moments $\mu_{\mathrm{eff}} \simeq 3\,\mu_{\mathrm{B}}$ on only a small fraction $f \simeq 0.02$ of Os sites. We suggest disorder-related effects, such as oxygen nonstoichiometry or site interchange between Os and Y ions, as the most likely explanation for the magnetic response of this material.

I. INTRODUCTION

In the single-ion picture, octahedrally coordinated transition-metal ions with a d^4 electronic configuration, such as Os^{4+} and Ir^{5+}, are expected to have a nonmagnetic singlet ground state. For strong spin-orbit coupling, the t_{2g} levels are split into a fully filled $j_{\mathrm{eff}} = 3/2$ quadruplet and an empty $j_{\mathrm{eff}} = 1/2$ doublet, yielding an overall $J_{\mathrm{eff}} = 0$, while for strong Hund's coupling, each site is in a $S = 1$, $L_{\mathrm{eff}} = 1$ state with L_{eff} and S coupled by the spin-orbit interaction in a $J_{\mathrm{eff}} = 0$ state. Since the d^4 ion is nonmagnetic in both of these limits, the singlet ground state is expected to be robust.

Such materials have been studied since the 1960s [1] and, although many are nonmagnetic, there are cases in which a magnetic moment and possibly magnetic ordering is nevertheless observed experimentally [2–10], with several different novel mechanisms being proposed to explain this [11–14]. Notable examples which have been studied recently include the double perovskite iridates A_2YIrO$_6$ ($A =$ Sr, Ba) [4–6] and the pyrochlore osmates R_2Os$_2$O$_7$ ($R =$ rare earth) [8]. For the iridates, some theories proposed that a novel excitonic mechanism related to the interplay of spin-orbit coupling and superexchange was behind the magnetic state [11–13]. It has been pointed out, however, that the superexchange interaction is probably not strong enough in the A_2YIrO$_6$ family to induce excitonic magnetism since the IrO$_6$ octahedra are isolated from one another [15]. Instead, the observed moment has been ascribed to extrinsic effects, such as paramagnetic impurities [6,7,16] and antisite disorder [14,16].

The pyrochlore osmates provide more promising candidates for excitonic magnetism since the OsO$_6$ octahedra form a corner-sharing network, meaning the superexchange is expected to be much larger. Less work has been done on this family of materials, with one experimental study on the $R =$ Y and Ho pyrochlores observing nonzero moments in both cases [8].

In this work, we add to previous studies on candidates for excitonic magnetism by reporting measurements on Y$_2$Os$_2$O$_7$ made with a variety of techniques, including AC and DC magnetic measurements, muon spin relaxation (μSR), and resonant inelastic x-ray scattering (RIXS). The interpretation of the data is informed by single-ion electronic structure calculations. We find that the observed paramagnetic moments undergo a bulk spin freezing at low temperatures that is similar to that found to occur in canonical spin glasses. Single-ion calculations based on the actual distorted crystal structure yield a $J_{\mathrm{eff}} = 0$ state in the intermediate-coupling regime and indicate that spin-orbit coupling, Hund's coupling, and the trigonal crystallographic distortion are all important in modeling the experimental spectra. We show that the field dependence of magnetization is explained by large moments $\mu_{\mathrm{eff}} \simeq 3\,\mu_{\mathrm{B}}$ on only a small fraction $f \simeq 0.02$ of Os sites, allowing us to conclude that the observed paramagnetic moment

---

*Present address: Los Alamos National Laboratory, Los Alamos, New Mexico 87545, USA.

†andrew.boothroyd@physics.ox.ac.uk
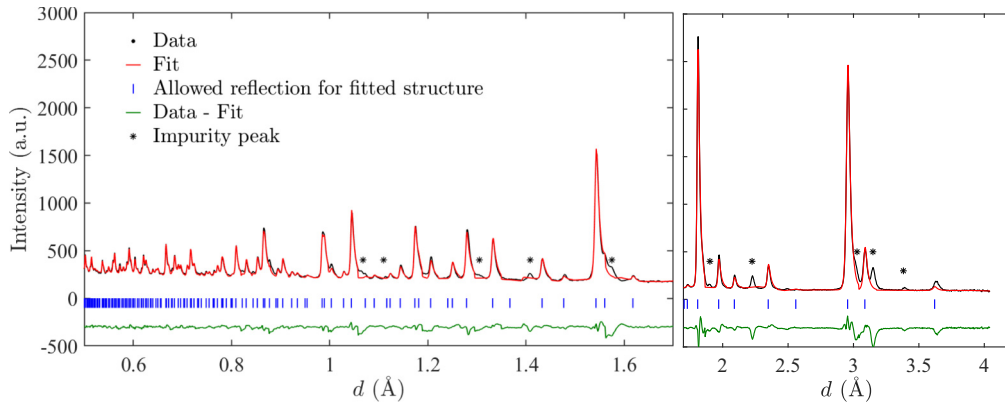
FIG. 1. Powder neutron diffraction from $Y_2Os_2O_7$ measured at a temperature of 200 K as a function of $d = 2\pi/Q$, where Q is the momentum transfer. The black squares are experimental data and the red line is the fitted profile after structural refinement (corresponding to the 200 K parameters in Table I). The green line beneath the ticks is the difference between the data and fit. The blue tick marks show the expected locations of peaks due to the main $Y_2Os_2O_7$ phase, while black asterisks indicate impurity peaks. When regions in which impurity peaks are present are excluded, the Bragg R factor for this fit is 6.54. The two panels show data from two different banks of the GEM detector.

is most likely related to crystalline disorder, such as oxygen nonstoichiometry or site mixing between Os and Y ions.

II. EXPERIMENTAL DETAILS

A 5.2 g polycrystalline sample of nominal composition $Y_2Os_2O_7$ was synthesised through a conventional solid-state reaction. A stoichiometric mixture of Y_2O_3 and OsO_2 (99.99% purity, obtained from Alfa Aesar) was ground and sealed in an evacuated quartz tube, which was then heated up to 773 K and left at this temperature for 24 hours. The product was reground and pressed into a pellet and sealed in a new quartz tube under vacuum. The quartz tube was heated slowly up to 1173 K and kept at this temperature for 2 days. The target phase was thus obtained after shutting off the furnace.

Elastic neutron-scattering measurements performed on the General Materials Diffractometer (GEM) beam line at the ISIS Facility [17] allowed for a full structural refinement, as shown in Fig. 1 and Table I, yielding lattice parameter $a = 10.225(1)$ Å at 200 K. Superficially, the refinement indicates an oxygen deficiency of approximately 1.5%, but this result is not significant as there is an uncertainty of around 2% in the scattering length of Os [18]. The only fractional coordinate in this structure which is not constrained by symmetry is the $48f$ oxygen-site x coordinate, which we find to be $x_{48f} = 0.3352(2)$ at 200 K. For reference, zero trigonal distortion of the OsO_6 octahedra corresponds to $x_{48f} = 5/16 = 0.3125$, with $x_{48f} > 5/16$ indicating trigonal compression of the octahedra in this case. The structural parameters are similar but

not identical to those reported in Ref. [8], with the variation possibly related to different levels of microscopic disorder resulting from the different sample synthesis routes. A small number of low-intensity peaks from an unidentified impurity phase can also be seen. These peaks could not be indexed by Y, Os, any known oxide of Y or Os, or any material expected to be close to the beam path [19]. Based on the intensity of the strongest peaks in the neutron-scattering spectrum, we estimate that the impurity is on the level of $\lesssim 6\%$ and note that the μSR, RIXS, and specific heat measurements presented in this work, being bulk probes, are expected to be relatively insensitive to this level of impurity. The potential effects of the impurity on magnetization will be discussed in Sec. III A.

DC magnetization measurements up to 16 T and specific-heat measurements were performed on a Quantum Design Physical Property Measurement System (PPMS), and AC and DC magnetization measurements up to 7 T were performed on a Quantum Design Magnetic Property Measurement System (MPMS). Muon-spin relaxation (μSR) measurements were performed in a ^{4}He cryostat (3.8–225 K) and a dilution refrigerator (92 mK–3.8 K) on the MuSR beam line at the ISIS Pulsed Muon Facility [20] on part of the powder sample packed in a 25 μm silver foil packet mounted on a silver backing plate. An additional measurement on the same sample was performed in a ^{4}He cryostat on the General Purpose Surface-Muon (GPS) Instrument spectrometer at the Paul Scherrer Institute (PSI) to check the low decay time spectrum at 1.5 K. Resonant inelastic x-ray Scattering (RIXS) data were

TABLE I. Refined structural parameters for $Y_2Os_2O_7$ in the space group $Fd\bar{3}m$. The numbers in parentheses are uncertainties on the refinement procedure. There is only one free fractional coordinate in this structure for the O on the $48f$ site (x_{48f}), corresponding to trigonal distortion of the oxygen octahedra around the Os site. Zero trigonal distortion corresponds to $x_{48f} = 5/16 = 0.3125$.

Temperature (K)	a (Å)	x_{48f}	O_{48f} occupancy (%)	$B_{iso}(Os)$ (Å^2)	$B_{iso}(Y)$ (Å^2)	$B_{iso}(O_{48f})$ (Å^2)	$B_{iso}(O_{8b})$ (Å^2)
200	10.225(1)	0.3352(2)	98.7(5)	0.46(2)	0.84(4)	0.91(3)	0.78(7)
100	10.222(1)	0.3354(2)	98.5(8)	0.42(3)	0.71(5)	0.83(5)	0.70(9)
2	10.220(1)	0.3355(2)	98.5(8)	0.41(3)	0.68(5)	0.81(5)	0.67(9)
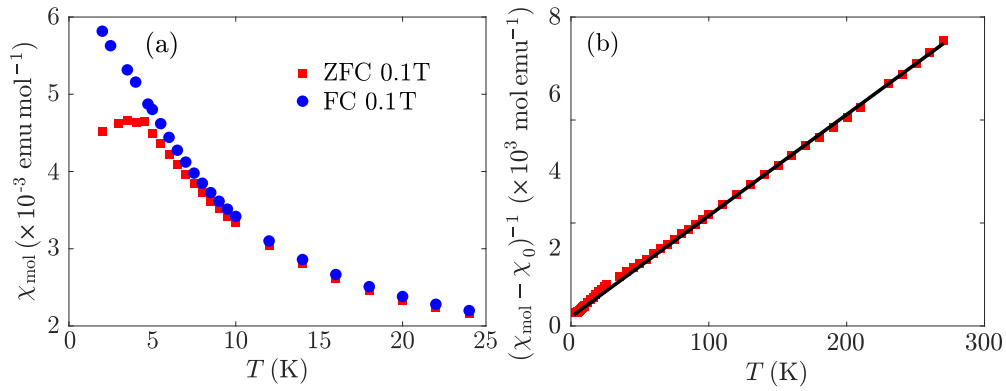
FIG. 2. (a) DC magnetic susceptibility of polycrystalline $Y_2Os_2O_7$. Data were taken using a 0.1 T measurement field, after cooling from room temperature in the measurement field (FC, red squares) and in zero field (ZFC, blue circles). (b) $(\chi_{\text{mol}} - \chi_0)^{-1}$ as a function of temperature, where χ_0 is the background susceptibility obtained in a Curie-Weiss fit of the form shown in Eq. (1). The black line is the result of this Curie-Weiss fit, showing good agreement with the data down to around 60 K. The resulting fit parameters are $\sqrt{f}\mu_{\text{eff}} = 0.417(1)\,\mu_{\text{B}}$, $\theta = -8.9(5)\,$K, and $\chi_0 = 8.96(1) \times 10^{-4}\,$emu mol^{-1}.

taken on a pressed pellet of the sample at the beam line ID20 of the European Synchrotron Radiation Facility [21].

III. RESULTS

A. DC magnetization

DC magnetic susceptibility data (Fig. 2) show Curie-Weiss-like behavior over a large temperature range with departures below about 60 K and a significant splitting between field-cooled and zero-field-cooled curves below about 5 K. For temperatures above 70 K, the data fits well to the form

$$\chi = \chi_0 + \frac{N_A f \mu_{\text{eff}}^2}{30 k_B (T - \theta)}, \tag{1}$$

where χ is the DC susceptibility expressed in centimeter-gram-second (CGS) units (emu mol^{-1}), f is the fraction of Os sites which exhibit a magnetic moment, and μ_{eff} is the effective moment due to each of these Os sites [Fig. 2(b)]. This yields $\sqrt{f}\mu_{\text{eff}} = 0.417(1)\,\mu_{\text{B}}$, a Curie-Weiss temperature of $\theta = -8.9(5)$ K, and a temperature-independent background susceptibility $\chi_0 = 8.96(1) \times 10^{-4}$ emu mol^{-1}. The formula unit for all molar quantities here and throughout this work is $Y_2Os_2O_7$, unless otherwise stated. The origin of the significant temperature-independent component of the susceptibility will be discussed in more detail in Sec. IV C in light of our RIXS results.

The observed DC magnetic susceptibility is similar to that reported in Ref. [8], where an effective moment of 0.49(2) μ_{B} and Curie temperature $-4.8(3)$ K were reported. The sample measured in that work contained 7% Y_2O_3 and 10% OsO_2 impurities, and the authors do not mention any unknown impurity similar to the one in our sample. The close similarity between the two samples from different sources and containing different secondary phases (albeit at low levels) indicates that the dominant features in the measured magnetization are from the $Y_2Os_2O_7$ phase. We will provide further evidence that the impurity does not affect the measured magnetization in Sec. IV via in-depth analysis of our μSR results.

Magnetization data taken up to 16 T at 2.5 K [Fig. 3(a)] show a small hysteresis (inset of figure). Due to the significant van Vleck susceptibility of this material, the moment μ is expected to be linear in H at high enough fields once the Curie-Weiss-like moments have reached saturation. We therefore subtract a van Vleck contribution corresponding to $\chi_0 = 8.96(1) \times 10^{-4}$ emu mol^{-1} consistent with the Curie-Weiss fit. The moment does not saturate up to the maximum field of 16 T, but it does appear to be approaching saturation [Fig. 3(b)]. We find that the observed rate of approach to saturation makes it unlikely that the saturated paramagnetic moment μ_{sat} exceeds 0.04 μ_{B} per Os site averaged over the whole sample.

The temperature dependence of the magnetization curves [Fig. 3(c)] shows that the moment does not exhibit normal paramagnetic behavior at low temperature. Instead, it is close to temperature independent at the lowest temperatures (2–5 K) with ideal paramagnetic behavior according to the Brillouin function (i.e., μ being a function of B/T only) not recovered up to 40 K.

The sample also shows a small but observable remanent magnetization and time-dependent relaxation when quenched from 7 T [Fig. 3(d)] at 2 K, with the moment not decaying fully even after many hours. The curve does not fit to a single exponential, consistent with a spread of decay times.

B. AC magnetization

In the real part of the AC susceptibility [Fig. 4(a)], a clear peak is seen close to the proposed spin-freezing temperature $T_{\text{f}} \simeq 5$ K (Ref. [8]), with the peak moving to lower temperatures and having a higher maximum χ' at lower frequencies. This shift in the peak position with frequency shows that there are slow magnetic dynamics in the 0.1–1000 Hz range. More quantitatively, we find that the peak shift is consistent with the relation

$$\Delta T_{\text{f}}/T_{\text{f,0}} = [T_{\text{f}}(\omega) - T_{\text{f}}(\omega \to 0)]/T_{\text{f}}(\omega \to 0)$$
$$= F\,\Delta(\ln \omega), \tag{2}$$
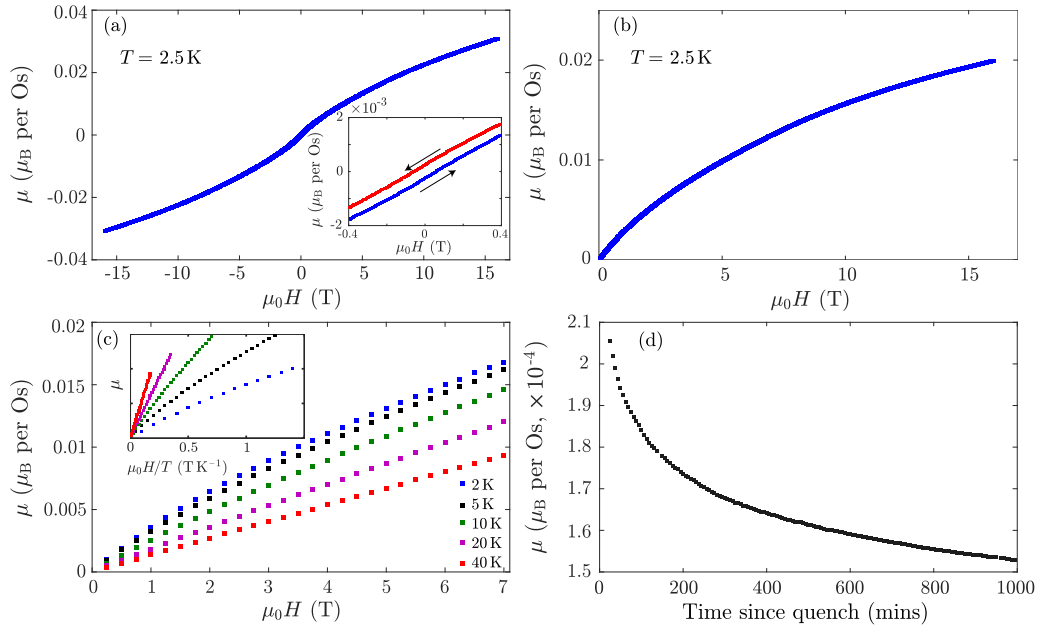
FIG. 3. (a) Magnetization μ of $Y_2Os_2O_7$ at 2.5 K as a function of applied field μ_0H. A small amount of hysteresis is seen between field-up and -down sweeps (inset). (b) The positive-field part of the dataset in (a) after subtraction of a linear van Vleck contribution $\chi_0 = 8.96(1) \times 10^{-4}$ emu mol^{-1}, consistent with the results of our Curie-Weiss fitting. (c) The temperature dependence of the magnetization between 2 and 40 K. The inset shows the same data as a function of μ_0H/T to demonstrate the lack of H/T scaling. (d) Remanent magnetization of $Y_2Os_2O_7$ at 2 K after quenching from a field of 7 T. In order to obtain this data, the superconducting magnet was ramped down from 7 T as quickly as possible over the course of around 6 minutes with the starting time $t = 0$ being when the field began to ramp down. The magnet was then heated up above its superconducting transition temperature and the first data point taken once the magnet reached its normal state.

with $F = 0.010(8)$ [Fig. 4(b)], which is within the range $F = 0.001$–0.08 found for typical spin glasses [22,23].

We found that the imaginary part of the AC susceptibility was smaller than the instrumental resolution of the magnetometer used for our measurements at all frequencies and temperatures measured, i.e., $\chi'' \lesssim 10^{-4}$ emu mol^{-1}. This weak χ'' is consistent with the behavior of known spin glasses and indicates a wide spread of relaxation times [23].

The hysteretic and frequency-dependent effects described here, including the splitting between field-cooled and zero-

field-cooled DC magnetization, AC magnetization, and remanence, are all characteristic features of canonical spin glasses and other spin-glass-like pyrochlore systems such as $Y_2Mo_2O_7$ [24,25].

C. Heat capacity

The zero-field specific heat of a pressed pellet made from the above sample is smooth at all temperatures down to 2 K and shows no obvious signature of the spin glass transition
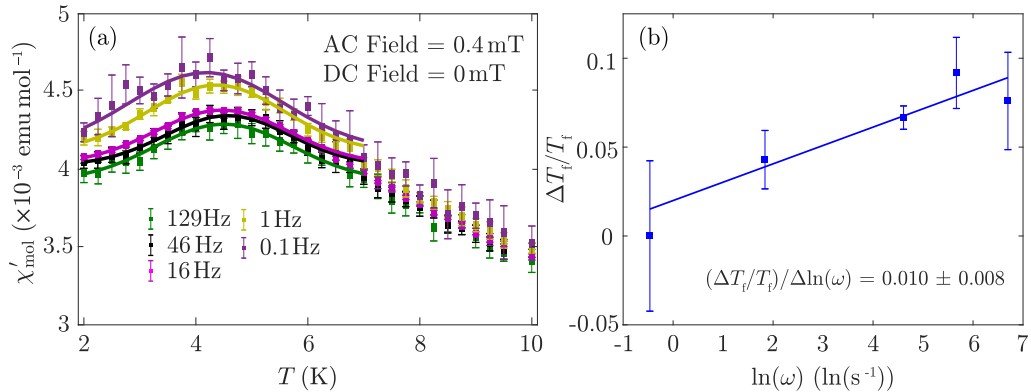
FIG. 4. (a) AC magnetic susceptibility of $Y_2Os_2O_7$ powder. Data were taken using a 0.4 mT AC measurement field and zero DC field after cooling from room temperature in zero field. χ'_{mol} is the real part of the AC molar susceptibility in CGS units. Solid lines are fits to a Gaussian peak plus a constant background in the region around 4 K to find the peak position for plotting in (b) and to emphasize its shift to lower temperature with decreasing frequency. (b) Fractional change in the peak position in the real part of the AC magnetic susceptibility, $\Delta T_f/T_{f,0} = [T_f(\omega) - T_f(\omega \to 0)]/T_f(\omega \to 0)$, as a function of $\ln(\omega)$, where $T_f(\omega)$ is taken from the fitted peaks in (a). The blue line is the best linear fit, yielding a gradient $\Delta T_f/T_f/\Delta\ln(\omega) = 0.010 \pm 0.008$, comparable to that seen in a typical spin glass [22].
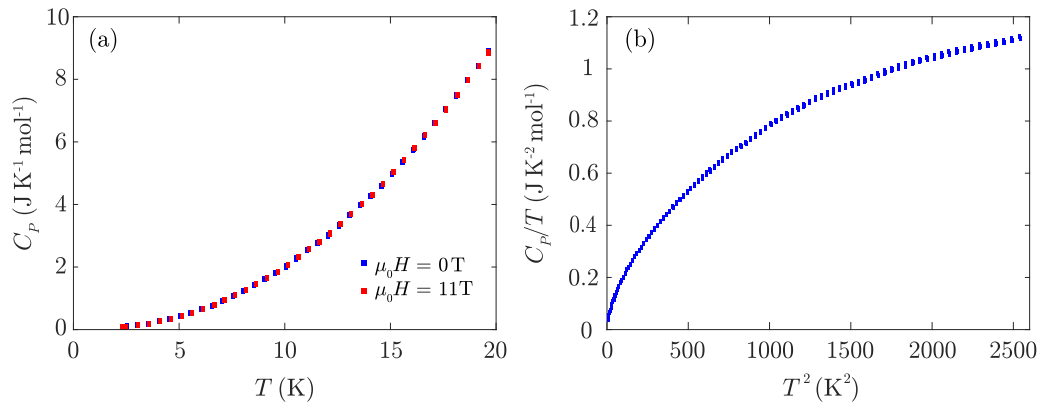
FIG. 5. (a) Molar specific heat of $Y_2Os_2O_7$ as a function of temperature in zero and high (11 T) magnetic field. (b) C/T as a function of T^2 in zero magnetic field.

or any other magnetic behavior [Fig. 5(a)]. A plot of C/T as a function of T^2 [Fig. 5(b)] shows that the data do not fit a simple Debye model ($C/T = \gamma + \alpha T^2$) over any measured temperature range.

Remarkably, on applying a large (11 T) magnetic field, we find no observable change in the specific heat of $Y_2Os_2O_7$ at any temperature, as shown in Fig. 5(a). Since such a large magnetic field can reasonably be expected to significantly affect the magnetic state—and hence the magnetic component of the heat capacity—it is very likely that the specific heat measured experimentally is almost entirely due to phonons, and any magnetic contribution is unresolvably small at all temperatures.

Although surprising, we find that the lack of an observed magnetic specific-heat signal is consistent with the results of the other measurements presented here. The effective moment per Os ($\sqrt{f}\mu_{\text{eff}}$) is quite small and the spin glass state likely has a large amount of residual disorder, so the entropy change associated with the spin-freezing transition may be quite low. Additionally, the release of entropy for typical spin glasses has been observed to be spread over a large temperature range up to around $5T_{\text{f}}$ [26], resulting in a very small contribution to the specific heat at any given temperature [27].

Our measurements of $Y_2Os_2O_7$ are consistent with the data presented by Zhou *et al.* in Ref. [8]. However, our conclusion that there is no observable magnetic contribution to the specific heat differs. We therefore performed further heat capacity measurements on a pellet of $Y_2Ti_2O_7$ as a nonmagnetic reference sample. For $Y_2Ti_2O_7$, we obtained virtually identical data to Zhou *et al.* up to 30 K. However, we find that after applying the same scaling, the zero-field specific heats of $Y_2Ti_2O_7$ and $Y_2Os_2O_7$ are not the same above 30 K, where any magnetic signal due to spin glass behavior should be small. The discrepancy between this finding and the conclusions of Ref. [8] indicates that $Y_2Ti_2O_7$ is not a sufficiently accurate nonmagnetic background sample to isolate the small magnetic contribution to the heat capacity.

D. Muon spin relaxation (μSR)

Zero-field μSR data measured at ISIS show very little relaxation of the implanted muons at high temperatures, $\gtrsim 100$ K (not shown), as expected for a paramagnet, with

relaxing behavior developing gradually on cooling below this point [Fig. 6(a)]. The relaxation becomes significantly greater below around 20 K as the spin-freezing temperature is approached, although the spectrum does not completely stop evolving even at the lowest measured temperature of 92 mK. This indicates that the evolution of magnetic fluctuations in this system is very gradual, as is typical for spin glasses. No oscillations are seen at any temperature, confirming that there is no long-range magnetic order, and additional datasets at 1.5 and 10 K taken at PSI with much higher time resolution confirm that there is no oscillatory behavior on shorter timescales down to 0.1 μs [Fig. 6(b)]. Overall, the data are remarkably similar to those seen in canonical spin glasses such as AgMn [28], supporting the assertion that some kind of spin freezing occurs in this material.

In an applied longitudinal field at 0.12 K [Fig. 6(c)], a significant proportion of the relaxation is decoupled at the smallest measured field of 20 mT, with no observable change between 80 and 160 mT. A similar longitudinal field dependence was also found at 2 K (not shown). It has been shown that the relaxation caused by a distribution of static internal fields can be quenched by an applied field that exceeds the internal fields by about a factor of 10 (Ref. [29]). Therefore, our observations suggest that there is a small ($\sim$1 mT) static (on the muon precession timescale) component of the internal field in $Y_2Os_2O_7$.

E. Resonant inelastic x-ray scattering (RIXS)

In Figs. 7(a) and 7(b), we show RIXS maps of the Os L_3 resonance measured at 15 K. In the lower-resolution map [Fig. 7(b)], the most significant feature is a high-intensity excitation peaked at energy transfer $\Delta E = 4.2$ eV and $E_i = 10.876$ keV. In the higher-resolution map [Fig. 7(a)], two excitations are seen clearly at energy transfers $\Delta E = 0.2$ eV and 0.7 eV, as well as a weaker, broad feature around $\Delta E = 1.00{-}1.25$ eV. Within the resolution of these data, all these lower-energy excitations resonate at the same incident energy $E_i = 10.8725$ keV. There are also some broad, weak excitations at energy transfers around 3.33 eV and above 5 eV. Cuts through all these features [Figs. 7(c) and 7(d)] show that no splitting into sublevels is resolvable in any of them.
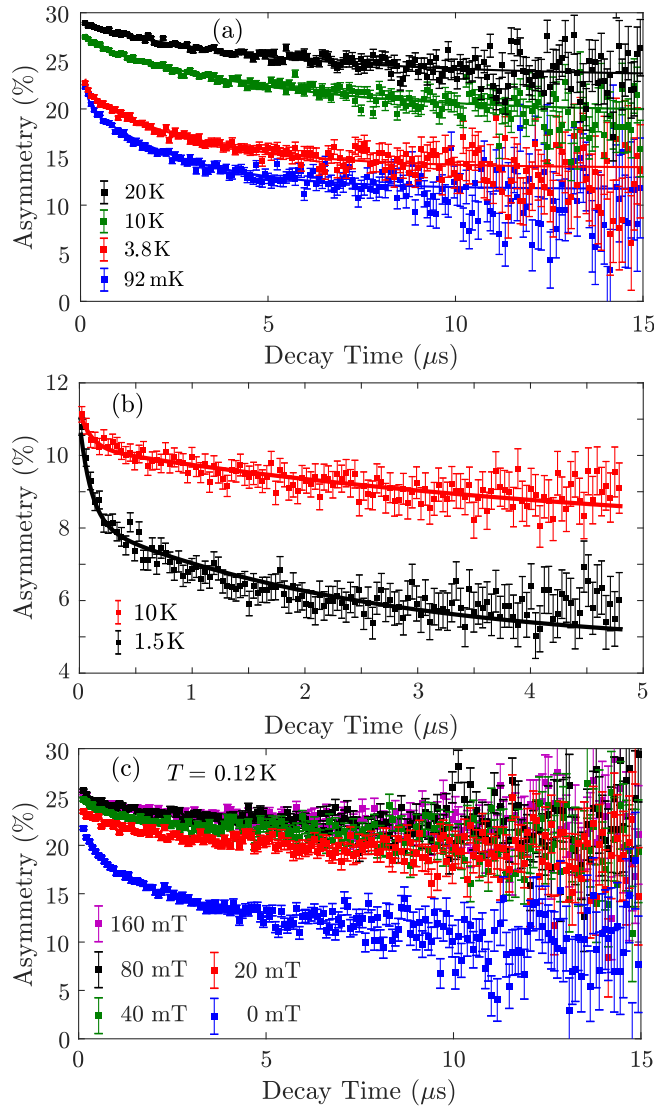
FIG. 6. (a) Measured muon decay asymmetry as a function of decay time at selected temperatures for polycrystalline $Y_2Os_2O_7$. Datasets at temperatures greater than 3.8 K were recorded in a ^{4}He cryostat, while those at 3.8 K and below were taken in a dilution refrigerator. Solid lines represent a double-exponential fit, as discussed in Sec. IV B. (b) Similar spectra to (a), but data taken at a different facility with higher time resolution to show that no structure has been missed in the low decay time region. This data was taken with the beam line's spin rotator switched on, leading to a lower absolute value of the measured asymmetry. (c) Muon decay asymmetry at 0.12 K as a function of longitudinal applied field.

As the incident photon energy is tuned to the Os L_3 edge, we assume that the observed excitations involve Os $5d$ states. The crystal field at the Os site is close to cubic with a small perturbing trigonal distortion, so to a first approximation we can identify the $\Delta E = 4.2$ eV feature with single-ion t_{2g}–e_g excitations and the low-energy features with intra-t_{2g} excitations. This assumption allows us to estimate the cubic crystal field parameter $10Dq = 4.2$ eV. This assignment is supported by the fact that the t_{2g}–e_g and intra-t_{2g} excitations resonate at energies separated by around 4 eV and that this crystal

field value is comparable to that found in other osmates, for example, $10Dq = 4.3$ eV in Ba_2YOsO_6 and $10Dq = 4.5$ eV in Ca_3LiOsO_6 [30].

To quantify the energies and widths of these RIXS excitations, we performed phenomenological fits of the spectra in Fig. 7, with the data in Figs. 7(c) and 7(d) modeled by a linear background and several Gaussian peaks. The corresponding fit parameters, numbered as indicated in the figures, are given in Table II.

IV. ANALYSIS

Our magnetization, heat capacity, and μSR results provide evidence for spin glass behavior in $Y_2Os_2O_7$ with a small average magnetic moment per Os site of about $0.4\,\mu_B$/Os, consistent with previous work (Ref. [8]). We shall now present analysis which shows that this moment is most likely associated with a small concentration of sites carrying large spins in a nonmagnetic host, as opposed to a small spin on every site.

A. Field-dependent magnetization

Assuming local moments with effective spin J, we can establish from the results of our Curie-Weiss fit that

$$\sqrt{f}g\sqrt{J(J+1)} = 0.417(1), \qquad (3)$$

where g is the g factor of the moment. We are unable to determine f, g, and J separately, but as the saturated moment

$$\mu_{\text{sat}} = fgJ\mu_B \qquad (4)$$

has a different dependence on f and J, we can use the field dependence of our magnetization data, together with assumptions derived from the observed spin glass behavior, to test the likelihood of different values of f.

For this analysis, we shall consider $f = 0.02$ and 1, chosen as representative of the scenarios in which the moments are dilute and concentrated, respectively. The lower value $f = 0.02$ is typical of the levels of intersite mixing and microscopic disorder reported in similar iridate materials [6].

For each f, we can use the constraint in Eq. (3) to eliminate one of g and J. Having done this, we can then calculate μ_{sat} as a function of the remaining variable using Eq. (4). In the discussion which follows, we shall assume J has been eliminated in this way, leaving μ_{sat} as a function of g alone; however, the analysis would proceed in the same way if we were to treat μ_{sat} as a function of J instead.

Plots of μ_{sat} as a function of g obtained this way are presented in Fig. 8(a) for $f = 0.02$, and Fig. 8(b) for $f = 1$. As discussed earlier, our magnetization data indicate that μ_{sat} does not exceed about $0.04\,\mu_B$, and so from Figs. 8(a) and 8(b) we see immediately that $g \gtrsim 2$ if $f = 0.02$, and $g \gtrsim 4$ for $f = 1$.

We now consider the implications of the spin glass regime. Normal paramagnetic behavior is not observed here (see Fig. 3), and we assume that μ as a function of H is governed instead by some average internal energy barrier ΔE comparable with the spin-freezing temperature $T_f = 5$ K, i.e., $\Delta E \simeq 5k_B$ [31]. At $T \ll T_f$, we expect that spins can overcome the energy barrier and align with an external field B provided
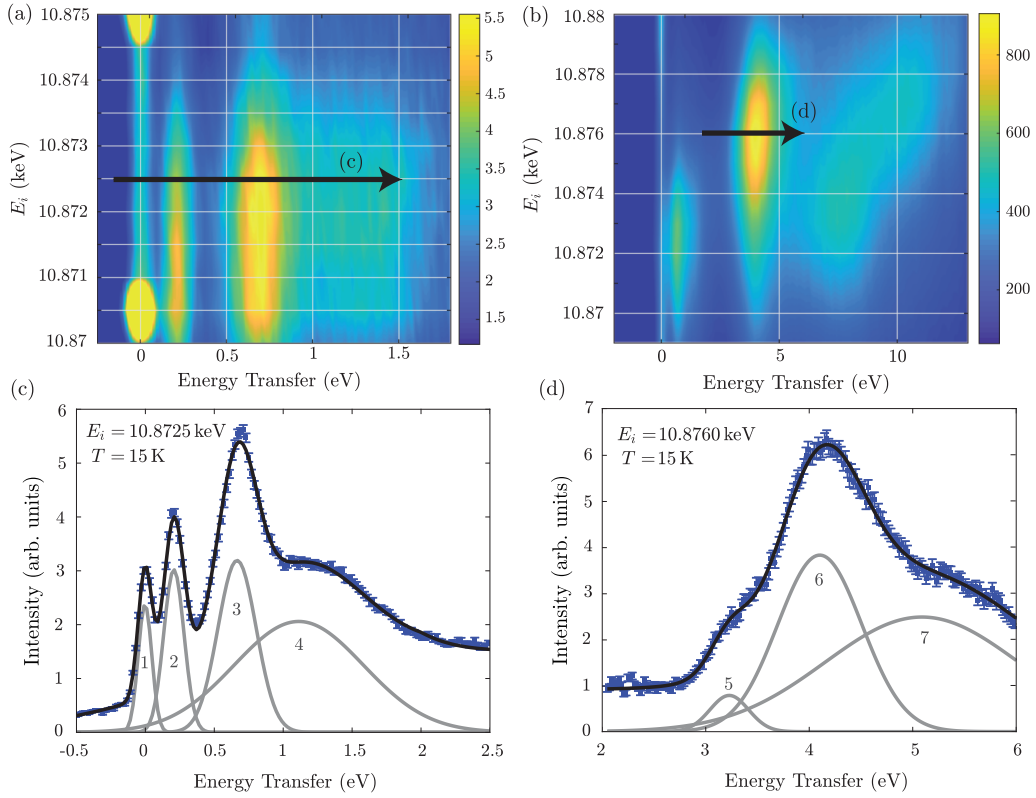
FIG. 7. RIXS spectra of $Y_2Os_2O_7$ taken at 15 K on the Os L_3 edge. (a) High-resolution map focusing on the low-energy excitations, (b) low-resolution map, (c) a cut through the low-energy excitations as marked in (a), and (d) a cut through the higher-energy excitation as marked in (b). The black lines are a fit to four Gaussian peaks plus a linear background in (c) and three Gaussians plus a constant background in (d), with parameters shown in Table II. Gray lines show the fitted Gaussian components with numbers corresponding to peak numbers in the table. The very strong peaks at zero energy in the maps are $Y_2Os_2O_7$ Bragg peaks.

$B \gg B_{\mathrm{c}}$, where

$$B_{\mathrm{c}} \simeq \Delta E / (gJ\mu_{\mathrm{B}}) \qquad (5)$$

is a crossover field. Figures 8(c) and 8(d) plot B_{c} as a function of g for $f = 0.02$ and $f = 1$, respectively, calculated from Eqs. (5) and (3). We take $B_{\mathrm{sat}}/10$ as a lower limit for B_{c}, where $B_{\mathrm{sat}} \simeq 10$ T is an estimate of the saturation field at $T = 0$ from Fig. 3, and we take the upper limit on B_{c} to be B_{sat}. Hence, we conservatively estimate B_{c} to be in the range $1 \lesssim B_{\mathrm{c}} \lesssim 10$ T.

TABLE II. Gaussian parameters obtained from a fit of the sum of four Gaussians plus a linear background to the RIXS spectra in Fig. 7(c), $i = 1$–4, and three Gaussians plus a constant background to Fig. 7(d), $i = 5$–7, where each Gaussian is of the form intensity $= a_i \exp[-(E - E_i)^2 / 2\sigma_i^2]$.

i	a_i	E_i (eV)	σ_i (eV)
1	470(20)	$-0.003(2)$	0.050(2)
2	600(20)	0.206(2)	0.073(3)
3	640(30)	0.665(4)	0.139(6)
4	410(10)	1.11(3)	0.47(2)
5	170(20)	3.23(2)	0.19(3)
6	820(40)	4.10(1)	0.41(2)
7	530(20)	5.08(6)	0.93(4)

The allowed range of g corresponding to this acceptable range of B_{c} is indicated in Figs. 8(c) and 8(d).

Figure 8 shows that there are values of g which are very improbable. These are represented by the darker shaded regions on the plots. For $f = 1$, we find that all values of g are very unlikely under these constraints, while for $f = 0.02$, the constraints are satisfied when $1.5 \lesssim g \lesssim 4$. Converting this range of g into a range of J using Eq. (3), we obtain $0.5 \lesssim J \lesssim 1.5$. Overall, we find that for $f = 0.02$, there is a wide range of physically reasonable g and J parameters consistent with the magnetization data, but for $f = 1$, no such combination of parameters exists.

It is noteworthy that since the calculated μ_{sat} and B_{c} are both a factor of 5–10 larger for $f = 1$ than for $f = 0.02$, the above arguments still hold for quite significant changes in f or in the experimental constraints. For example, any value of $f \lesssim 0.1$ still yields some plausible values of g, whereas any $f \gtrsim 0.5$ leads to all values of g being unlikely based on experiment. We therefore conclude that the fraction of occupied Os sites is very likely to be of the order of a few %, with the majority of Os sites adopting a nonmagnetic state.

B. Muon-spin relaxation (μSR)

Having established that the spins in the sample are very likely to be dilute, we now perform fitting and simulations of the spin-glass-like relaxation in our μSR spectra.
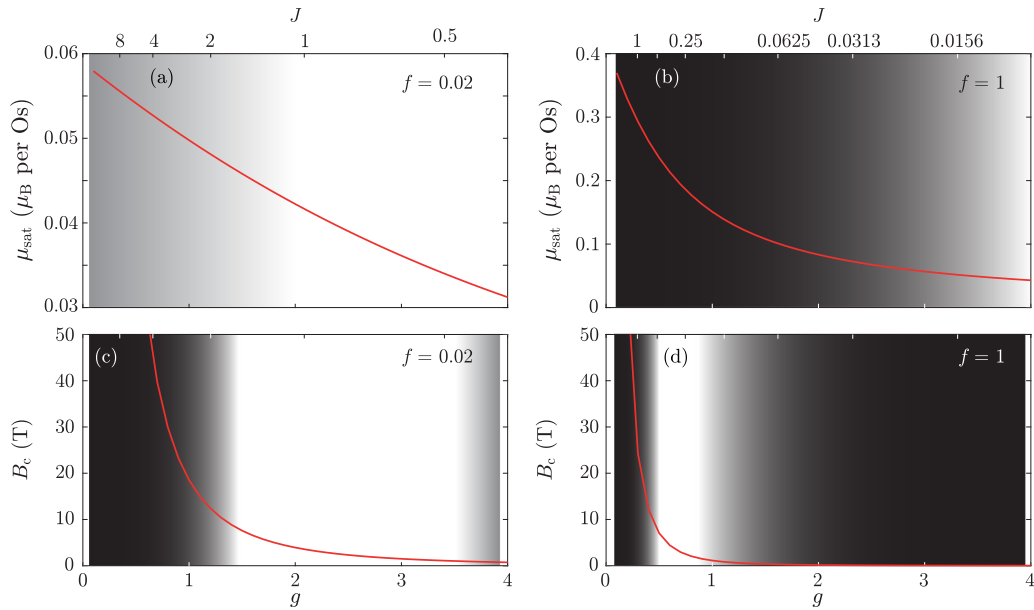
FIG. 8. (a),(b) The calculated saturated moment $\mu_{\mathrm{sat}} = fgJ\mu_{\mathrm{B}}$ as a function of J (top axis) and g (bottom axis) for two plausible values of f, found by solving Eqs. (3) and (4) as described in the main text. (c),(d) The calculated crossover field $B_{\mathrm{c}} = 5k_{\mathrm{B}}/gJ\mu_{\mathrm{B}}$ as a function of g and J, found by solving Eqs. (3) and (5) as described in the main text. The g and J axes are identical for plots at the same f. The gray shading indicates regimes of g, which imply saturation magnetizations (top panels) or saturation fields (bottom panels) that would be in poor agreement with our measurements (see text for a detailed discussion).

1. Fitting

At all temperatures, the μSR asymmetry appears to consist of a relaxing part plus a constant baseline component which does not relax even at long decay times, with the relative magnitudes of these two parts varying significantly with temperature. In order to quantify this, we performed fits to the sum of two exponentials plus the baseline asymmetry, $A(t) = A_{\mathrm{b}} + A_{\mathrm{r}}[(1-a)e^{-\lambda_1 t} + ae^{-\lambda_2 t}]$ at each temperature where A is the observed muon decay asymmetry, t is the decay time, λ_1 and λ_2 are the two exponential decay rates, A_{r} is relaxing asymmetry due to muons experiencing a B field in the sample, and A_{b} is the baseline asymmetry from muons which do not experience a magnetic field. A_{b} includes muons which stop in the sample holder, cryostat/dilution refrigerator, and any nonmagnetic or paramagnetic parts of the sample. Throughout this procedure, the initial asymmetry $A_{\mathrm{i}} = A_{\mathrm{r}} + A_{\mathrm{b}}$ was held constant at $A_{\mathrm{i}} \simeq 30\%$ for the ^{4}He cryostat and at $A_{\mathrm{i}} \simeq 28\%$ for the dilution fridge. These values were found by fitting the initial asymmetry to the highest-temperature dataset available for each sample environment since A_{i} should only be a function of the muon beam polarization and sample environment and is not expected to change with temperature. For datasets above 40 K, we found that the spectrum fitted well to a single exponential so, at these temperatures, a was fixed at 0, while for lower temperatures, the full double-exponential form was required. The best possible fit was obtained by fixing $\lambda_2 = 9.66\,\mu\mathrm{s}^{-1}$ to its value in the lowest-temperature dataset in each sample environment for all double-exponential fits.

Physically, exponential relaxation can result from a dilute distribution of static moments [32] or dynamic moments with a single correlation time within the resolution of the

spectrometer [33]. The observation of two distinct exponential components may have a range of explanations, including two different muon stopping sites, two different magnetic phases, or two distinct correlation times for dynamic moments. Alternatively, the double-exponential fit may be a phenomenological fit to a more complex distribution of internal fields and relaxation times.

The temperature dependences of the double-exponential fit parameters are presented in Fig. 9. The relaxation rate λ_1 shows behavior which is reminiscent of that seen in other spin glasses [28,34], with an increase on cooling up to a peak at the spin glass temperature followed by a plateau below this point. The spin-freezing temperature T_{f} is $\simeq 3$ K based on this measurement, which is slightly lower than that seen in AC susceptibility. This discrepancy may be due to the different fluctuation timescales probed by the different techniques.

The baseline asymmetry shows a clear decrease on cooling before flattening out below T_{f}, except for a jump at 3.8 K which can be attributed to the change of sample environment from ^{4}He cryostat to dilution refrigerator at this temperature. This temperature dependence indicates that the volume of the sample which is in a paramagnetic state decreases only gradually on cooling with no particularly sharp change at any temperature. A possible explanation for this would be if spins in different parts of the sample are freezing at slightly different temperatures, which is plausible behavior for a spin glass.

Overall, it is very likely that the relaxing portion of the μSR spectrum is caused by the same part of the sample as the dilute spins which show hysteretic, spin-glass-like behavior in magnetization measurements. Since the muons can be assumed to stop randomly throughout the $Y_2Os_2O_7$
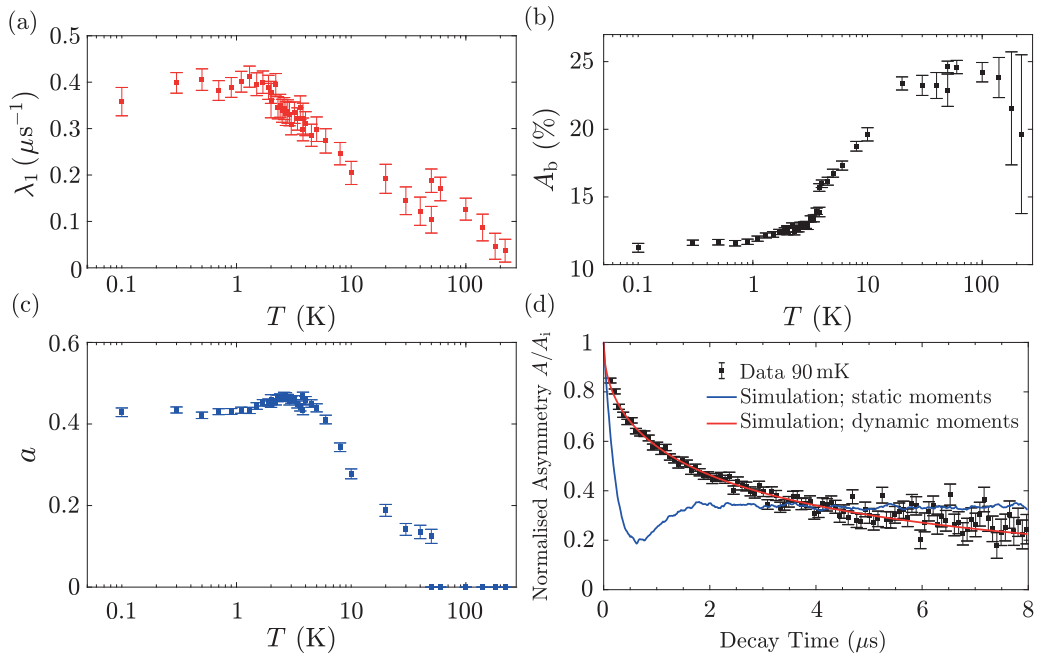
FIG. 9. (a)–(c) Temperature dependence of the slower exponential relaxation rate λ_1, fraction of the faster relaxation a, and the background asymmetry A_b fitted to our μSR data by the procedure outlined in the main text. (d) Simulated μSR spectrum at 90 mK for static and dynamic moments with moments of magnitude 2.95 μ_B on 2% of Os sites.

and impurity phases, we can therefore use the magnitude of the relaxing μSR signal A_r relative to the background A_b to examine which of the two phases the spins are located in.

Muons stop randomly in the impurity and $Y_2Os_2O_7$ phases in proportion to their volume, and it is reasonable to assume that muons stopping in the $Y_2Os_2O_7$ would not couple significantly to magnetic fluctuations in the impurity phase. Since the impurity is only a few % of the sample by volume, the relaxing asymmetry A_r would therefore be much smaller than the baseline asymmetry A_b if the impurity were the source of spin glass behavior. At low temperature, the baseline asymmetry A_b is similar in value to the relaxing asymmetry A_r (e.g., $A_r = 13.4\%$ and $A_b = 11.4\%$ at 92 mK). We therefore find that a magnetic impurity phase cannot be the source of the observed spin glass behavior.

If the spins are located in the $Y_2Os_2O_7$ phase, magnetic exchange mediated by ions located between the spins and the muon stopping sites in this phase would likely cause a significant magnetic field at the muon site. For example, in the double perovskite iridates, it has been shown that exchange mediated by Y^{3+} and O^{2-} ions is significant even between second- and third-nearest-neighbor Ir sites [16]. Furthermore, simulations presented in Ref. [16] show that for a double perovskite lattice populated with a few % spins on one of the octahedral sites, the majority of Ir sites are no further than the third-nearest-neighbor distance from a spin. Assuming that similar results hold for the pyrochlore structure of $Y_2Os_2O_7$, muons stopping at most locations within the $Y_2Os_2O_7$ phase will experience a significant magnetic field even if the spin concentration is low. We therefore conclude that the relaxing behavior is consistent with dilute moments in the main $Y_2Os_2O_7$ phase, and that the impurity phase shows no noticeable signal other than a constant background in μSR.

2. Simulations

For the lowest-temperature dataset, we have performed a simulation similar to that presented in Ref. [35] to try to extract information about the spin dynamics. This simulation involves randomly populating a lattice with magnetic moments μ on a fraction f of the sites, then examining the internal field at a muon test site.

If the spins are assumed to be completely static, the simulation results in an asymmetry, which can be approximated by

$$A(t) = \int p(\Delta)\left[\frac{1}{3} + \frac{2}{3}\cos(\Delta t)\right]d\Delta, \qquad (6)$$

where Δ/γ_μ is the width of the field distribution at the muon site, $p(\Delta)$ is the probability of finding that field width for a randomly chosen muon site, and $\gamma_\mu = 2\pi \times 135.5$ MHz T^{-1} is the gyromagnetic ratio of the muon [29]. The simulated spectrum assuming the most likely values of $f = 0.02$ and $\mu = 2.95 \mu_B$ is presented in Fig. 9(d); however, we find that this model cannot reproduce the data for any values (f, μ).

If the spins are allowed to fluctuate, the model asymmetry becomes

$$A(t) = \int p(\Delta)e^{-2\Delta^2 t/\nu}d\Delta, \qquad (7)$$

where ν is the fluctuation rate [29]. The model with fluctuations provides a much better fit to the data. For $\mu \simeq 2.95 \mu_B$ and $f \simeq 0.02$, the best fit is achieved with $\nu \simeq 21$ MHz, as plotted in Fig. 9(d). This fit is, however, reliant on an adjustment of A_b from the previously fitted value of 11% to $\simeq 7\%$. If the baseline asymmetry is fixed at 11%, we find that the model cannot reproduce the data even in the dynamical case. This indicates either that the data is not well modeled by this scenario or that even at the lowest tempera-

tures, a significant fraction ($\simeq$18%) of muons stopping in the sample experiences a nonmagnetic or paramagnetic environment. Given that we have ruled out impurities on the >10% level, this latter situation would imply that the $Y_2Os_2O_7$ phase still contains some nonmagnetic regions even well below T_f.

C. RIXS single-ion calculations

It is reasonable to assume RIXS is sensitive to all Os sites in the sample, the majority of which we have now established to be nonmagnetic based on the above analysis of our other experimental results. We therefore performed single-ion calculations assuming the d^4 electronic configuration for the Os ions, including interelectron interactions, spin-orbit interaction, and trigonal crystal field terms in the Hamiltonian in order to understand the origin of the excitations seen in RIXS. This procedure is outlined in Refs. [36,37] and involves writing each contribution to the Hamiltonian as a matrix using the properly antisymmetrized multielectron states of the d^4 configuration as a basis, then numerically diagonalizing the combined Hamiltonian. The interelectron interaction is written in terms of Racah parameters [38] A, B, and C which can be transformed into intra- and interorbital Coulomb interactions U and U' and the effective Hund's coupling J_H via

$$\begin{aligned} J_H &= 3B + C, \\ U &= A + 4B + 3C, \\ U' &= A - 2B + C. \end{aligned} \tag{8}$$

Following Ref. [39], the crystal field is parametrized by Dq, $D\sigma$, and $D\tau$, where Dq represents the octahedral crystal field, and $D\tau$ and $D\sigma$ are small trigonal distortions away from the perfect octahedral case [40]. The parameters Dq, $D\sigma$, and $D\tau$ used in this work correspond to the parameters with the same symbols in Ref. [39]. The spin-orbit coupling strength enters via a single parameter ζ_{SO}.

Some of the above parameters could be found from experiment before performing calculations. We have estimated from the RIXS data that $10Dq = 4.2$ eV, and there is a direct relationship between $D\tau$, the sign of $D\sigma$, and the $48f$ oxygen position $x = 0.3352(2)$ [41,42], which yields $D\tau = -0.090$ eV and tells us that $D\sigma$ must have the same sign (−) as $D\tau$. The Racah parameter A only appears on the diagonal elements of the Hamiltonian and causes only a constant shift of all energy levels. Since spectroscopy reveals only relative, not absolute, energies, A is not determined by this measurement.

All other parameters (B, C, ζ_{SO}, and $|D\sigma|$) are, in general, free and ideally would be fitted to experimental data. Unfortunately, we do not observe enough excitations in the experiment for this to be possible in this case. Instead, we need to fix some of the parameters to values obtained from other, similar compounds.

We fixed the values of $\zeta_{SO} = 0.32$ eV and $B = 0$ to the values obtained for Ba_2YOsO_6 in Ref. [30] leaving as free parameters $D\sigma$ and $C = J_H$. Figures 10(a) and 10(b) show the results of this calculation, in which the best agreement with experiment is obtained for $D\sigma = -0.09$ eV and a region around $J_H/\zeta_{SO} \simeq 1.4$. All of the experimental peaks are consistent with one or more excitations in the calculation, although

notably many of the experimental features are in fact a combination of several closely spaced levels which are unresolved. There are several states (for example, those at 0.3 and 0.5 eV) which fall close to the edges of the experimental peaks, as well as one set of nearly degenerate states at around 2.1 eV which is not close to any feature in the experiment. It is possible that these states may have a low spectral weight if a full RIXS calculation were performed, in which case they would be unresolvable above the background, especially in the case of the 0.3 and 0.5 eV levels which may easily be swamped by the nearby, stronger excitations or combined with them via intersite hopping terms, which are not included in this model.

Changing $D\sigma$ causes small perturbations to the low-lying energy levels and makes the agreement with experiment less good. The $D\sigma = 0$ case is presented in Fig. 10(f) for comparison, showing how agreement is still close but slightly worse, in particular for the two lowest-energy observed peaks.

The above results are consistent with work on other osmates and iridates which has found $J_H \simeq \zeta_{SO}$ [30,43,44]. We emphasize that because of the number of free parameters and the inherent uncertainty due to the unknown RIXS matrix elements, we cannot conclude that the parameter values suggested here are definitely the values in this material, only that based on our current knowledge the present model is capable of explaining the data for plausible values of all parameters.

We also performed calculations by removing in turn the trigonal distortion [$D\tau = D\sigma = 0$, Fig. 10(c)], spin-orbit interaction [$\zeta_{SO} = 0$, Fig. 10(d)], and interelectron interactions [$B = C = 0$, Fig. 10(e)]. In all three cases, we could not find any values of the remaining parameters which adequately reproduce the two lowest-lying features at 200 and 700 meV in the RIXS spectrum. This allows us to conclude that all three effects (trigonal distortion, spin-orbit coupling, and interelectron interactions) are required to model the physics of this material.

The ground state for our likely set of parameters, as well as for *any* set of parameters calculated here as long as $J_H/\zeta_{SO} \lesssim 3$, is a $J_{eff} = 0$ nonmagnetic singlet. This allows us to rule out any kind of single-ion physics, including the trigonal distortion, as the source of the magnetic moment, consistent with our conclusions from other techniques.

For all reasonable sets of parameters, there are low-lying excitations in the 200–400 meV region, which may be either a doublet, triplet, or closely spaced singlet and doublet. Significantly, we find that for the trigonally distorted parameters found here ($D\tau = D\sigma = -0.09$ eV), these lowest-lying excitations are a singlet at 200 meV and a degenerate doublet at 300 meV. This is in contrast to the undistorted case where the first excitation is a triplet. Quantitative theories of excitonic magnetism applied to the A_2YIrO_6 (A = Sr, Ba) materials such as Ref. [11] are based on a situation where the first excited state is a low-lying triplet. In the scenario proposed here for $Y_2Os_2O_7$, the splitting between the singlet and doublet excitations is $\simeq$50% of the separation between the singlet excitation and the ground state, representing quite a significant departure from the scheme used in the theories. The theories may therefore need modification before being directly applied to the pyrochlore osmates.

In light of these calculations, we can now also explain the temperature-independent component of the magnetic
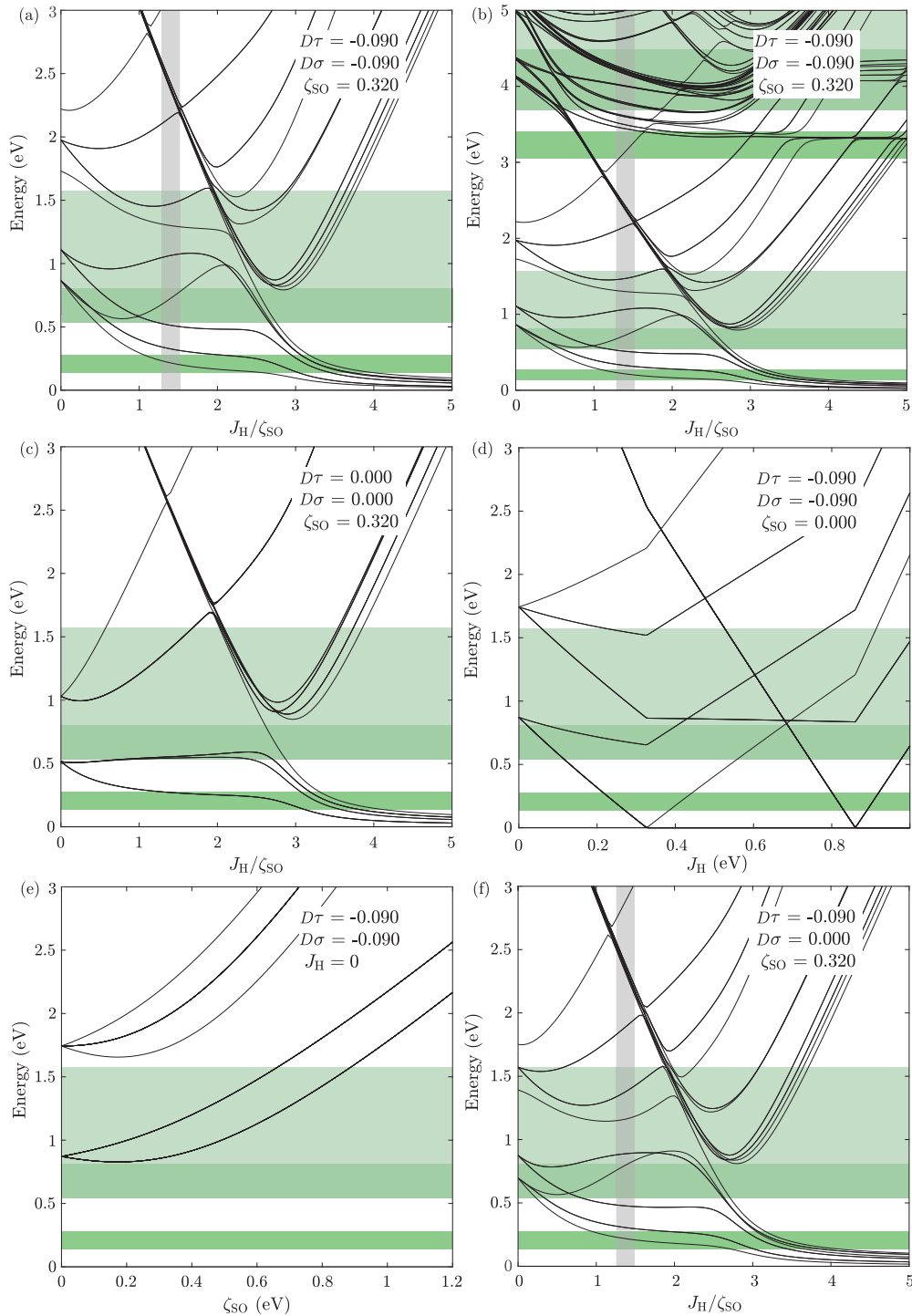
FIG. 10. The predicted energy levels of Os $5d^4$ electrons from single-ion calculations as outlined in the main text. Green horizontal stripes represent the observed energy levels in the present RIXS experiments with the position and width of the strip corresponding to the Gaussian peak position and full width at half maximum from Table II. Vertical gray stripes in (a) and (b) indicate a region where the calculated low-energy levels appear to best match those seen in experiment, as discussed in the main text, while the gray stripe in (f) is in the same position as those in (a) and (b) to aid visual comparison. (a) Calculation with nonzero trigonal distortion, spin-orbit interaction, and Hund's coupling. (b) Same as (a), but extended to high-energy transfer. (c) Calculation with no trigonal distortion. (d) Calculation with no Hund's coupling. (e) Calculation with no spin-orbit interaction. (f) Calculation with the variable trigonal distortion parameter $D\sigma$ set to zero.

susceptibility in Fig. 2. It was shown in Refs. [11,14] for $\mathrm{Ba_2YIrO_6}$ that following standard second-order perturbation theory, in the single-ion case the magnetic susceptibility of a system with a singlet ground state and a low-lying triplet

excited state at 350 meV is temperature independent and of the order of $\chi_0 \sim 1 \times 10^{-3}$ emu mol^{-1}. For $\mathrm{Y_2Os_2O_7}$, the first and second excited states are a singlet and a doublet, respectively, with a similar average energy above the ground

state as the triplet in Ba_2YIrO_6. The van Vleck susceptibility for $Y_2Os_2O_7$ is therefore expected to be of similar magnitude to that of Ba_2YIrO_6, consistent with our observed value of $8.96(2) \times 10^{-4}$ emu mol^{-1}.

V. DISCUSSION

When all of our experimental results are considered together, a consistent picture emerges with the majority of Os sites in a nonmagnetic $J_{eff} = 0$ state along with a few sites exhibiting a large spin. These magnetic defect sites are likely caused by some kind of microscopic disorder, for example, related to oxygen deficiency in the sample, site disorder involving partial interchange of Y^{3+} and Os^{4+} ions, or partial static charge disproportionation ($2 Os^{4+} \rightarrow Os^{3+} + Os^{5+}$).

This scenario is very similar to that proposed recently [16] for the $5d^4$ iridate Ba_2YIrO_6, for which it was shown via electron spin resonance (ESR) spectroscopy that the observed magnetic moment is caused by a small percentage of Ir^{6+} ($5d^3$) and Ir^{4+} ($5d^5$) magnetic defects, with the majority of Ir sites remaining in the nonmagnetic Ir^{5+} ($5d^4$) configuration. A similar scenario in $Y_2Os_2O_7$ would be consistent with all of our data; for example, only 1% of Os sites in the spin-only $5d^3$ configuration ($L = 0, J = S = 3/2$) would lead to $\sqrt{n}\mu_{eff} = 0.39 \mu_B$, very close to our measured value of $\sqrt{n}\mu_{eff} = 0.42 \mu_B$.

The authors of Ref. [16] also show that medium- and long-range interactions, possibly involving exchange mediated by Y ions, are significant in Ba_2YIrO_6 and that the magnetic defects tend to form extended correlated clusters even at low concentrations. Such long-range interactions and clustering of magnetic defects would provide a natural explanation for the spin freezing in $Y_2Os_2O_7$, including the observation in our μSR that the proportion of the sample exhibiting nonmagnetic behavior reduces gradually with temperature, and that some regions of the sample appear nonmagnetic even below T_f.

Our explanation for the magnetic behavior of $Y_2Os_2O_7$ is different from that proposed in Ref. [8]. Both we and the authors of Ref. [8] agree that Os in $Y_2Os_2O_7$ has a $J_{eff} = 0$ ground state. However, in Ref. [8], it is proposed that the magnetism is induced in the $J_{eff} = 0$ ground state by superexchange, which would imply a small moment on every Os site, whereas our analysis points to a small concentration of relatively large, defect-induced Os moments.

VI. CONCLUSION

This study has two principal conclusions. First, we show from RIXS measurements in conjunction with single-ion energy-level calculations that the majority of Os sites in $Y_2Os_2O_7$ host Os^{4+} ions with $5d^4$ electronic configuration and $J_{eff} = 0$ nonmagnetic singlet ground state in the single-ion picture. Second, we find that the observed effective magnetic moment and spin-freezing behavior is most likely caused by large moments $\sim 3 \mu_B$ located on a small proportion $\sim 2\%$ of Os sites, perhaps related to oxygen deficiency or structural disorder in the sample. This is a similar picture to that recently proposed by Fuchs *et al.* (Ref. [16]) for the $5d^4$ ion Ir^{5+} in Ba_2YIrO_6, and implies that the mechanism of excitonic magnetism does not apply to $Y_2Os_2O_7$.

[1] A. Earnshaw, B. N. Figgis, J. Lewis, and R. D. Peacock, J. Chem. Soc. **0**, 3132 (1961).

[2] E. Ramos, I. Alvarez, R. Sáez-Puche, M. Veiga, and C. Pico, J. Alloys Compd. **225**, 212 (1995).

[3] J.-C. Wang, J. Terzic, T.-F. Qi, F. Ye, S.-J. Yuan, S. Aswartham, S. V. Streltsov, D. I. Khomskii, R. K. Kaul, and G. Cao, Phys. Rev. B **90**, 161110(R) (2014).

[4] G. Cao, T.-F. Qi, L. Li, J. Terzic, S.-J. Yuan, L. E. DeLong, G. Murthy, and R. K. Kaul, Phys. Rev. Lett. **112**, 056402 (2014).

[5] L. T. Corredor, G. Aslan-Cansever, M. Sturza, K. Manna, A. Maljuk, S. Gass, T. Dey, A. U. B. Wolter, O. Kataeva, A. Zimmermann, M. Geyer, C. G. F. Blum, S. Wurmehl, and B. Büchner, Phys. Rev. B **95**, 064418 (2017).

[6] T. Dey, A. Maljuk, D. V. Efremov, O. Kataeva, S. Gass, C. G. F. Blum, F. Steckel, D. Gruner, T. Ritschel, A. U. B. Wolter, J. Geck, C. Hess, K. Koepernik, J. van den Brink, S. Wurmehl, and B. Büchner, Phys. Rev. B **93**, 014434 (2016).

[7] F. Hammerath, R. Sarkar, S. Kamusella, C. Baines, H.-H. Klauss, T. Dey, A. Maljuk, S. Gaß, A. U. B. Wolter, H.-J. Grafe, S. Wurmehl, and B. Büchner, Phys. Rev. B **96**, 165108 (2017).

[8] Z.-Y. Zhao, S. Calder, A. A. Aczel, M. A. McGuire, B. C. Sales, D. G. Mandrus, G. Chen, N. Trivedi, H.-D. Zhou, and J.-Q. Yan, Phys. Rev. B **93**, 134426 (2016).

[9] B. Ranjbar, E. Reynolds, P. Kayser, B. J. Kennedy, J. R. Hester, and J. A. Kimpton, Inorg. Chem. **54**, 10468 (2015).

[10] J. Terzic, H. Zheng, F. Ye, H.-D. Zhao, P. Schlottmann, L. E. De Long, S.-J. Yuan, and G. Cao, Phys. Rev. B **96**, 064436 (2017).

[11] G. Khaliullin, Phys. Rev. Lett. **111**, 197201 (2013).

[12] O. N. Meetei, W. S. Cole, M. Randeria, and N. Trivedi, Phys. Rev. B **91**, 054412 (2015).

[13] S. Bhowal, S. Baidya, I. Dasgupta, and T. Saha-Dasgupta, Phys. Rev. B **92**, 121113(R) (2015).

[14] Q. Chen, C. Svoboda, Q. Zheng, B. C. Sales, D. G. Mandrus, H.-D. Zhou, J.-S. Zhou, D. McComb, M. Randeria, N. Trivedi, and J.-Q. Yan, Phys. Rev. B **96**, 144423 (2017).

[15] K. Pajskr, P. Novák, V. Pokorný, J. Kolorenč, R. Arita, and J. Kuneš, Phys. Rev. B **93**, 035129 (2016).

[16] S. Fuchs, T. Dey, G. Aslan-Cansever, A. Maljuk, S. Wurmehl, B. Büchner, and V. Kataev, Phys. Rev. Lett. **120**, 237204 (2018).

[17] W. Williams, R. Ibberson, P. Day, and J. Enderby, Phys. B: Condens. Matter **241**, 234 (1997).

[18] V. F. Sears, Neutron News **3**, 26 (1992).

[19] The purity of the starting materials ensures that only Y, Os and O are present in the sample. We have searched the Inorganic Crystal Structure Database (ICSD) for all known compounds containing these three elements. We have thus ruled out Y, Os, Y_2O_3, OsO_2, and OsO_4. Based on the structures of La_3OsO_7, $La_3Os_2O_{10}$, and $La_4Os_6O_{19}$, we have furthermore ruled out the as-yet unreported materials Y_3OsO_7, $Y_3Os_2O_{10}$, and $Y_4Os_6O_{19}$. $YOsO_3$ and Y_2OsO_4 are not expected to form, but we have ruled them out based on models of $Sr/Ba/LiOsO_3$ and Na_2OsO_4. We have furthermore ruled out Al from the sample holder and environment as sources of the impurity.

[20] P. J. C. King, R. de Renzi, S. P. Cottrell, A. D. Hillier, and S. F. J. Cox, Phys. Scr. **88**, 068502 (2013).

[21] M. Moretti Sala, K. Martel, C. Henriquet, A. Al Zein, L. Simonelli, C. J. Sahle, H. Gonzalez, M.-C. Lagier, C. Ponchut, S. Huotari, R. Verbeni, M. Krisch, and G. Monaco, J. Synchrotron Radiat. **25**, 580 (2018).

[22] M. Gatteschi, R. Sessoli, and J. Villain, *Molecular Nanomagnets* (Oxford University Press, Oxford, 2006).

[23] M. Bałanda, Acta Phys. Pol. A **124**, 964 (2013).

[24] N. P. Raju, E. Gmelin, and R. K. Kremer, Phys. Rev. B **46**, 5405 (1992).

[25] S. R. Dunsiger, R. F. Kiefl, K. H. Chow, B. D. Gaulin, M. J. P. Gingras, J. E. Greedan, A. Keren, K. Kojima, G. M. Luke, W. A. MacFarlane, N. P. Raju, J. E. Sonier, Y. J. Uemura, and W. D. Wu, Phys. Rev. B **54**, 9019 (1996).

[26] K. Binder and A. P. Young, Rev. Mod. Phys. **58**, 801 (1986).

[27] L. E. Wenger and P. H. Keesom, Phys. Rev. B **13**, 4053 (1976).

[28] A. Keren, P. Mendels, I. A. Campbell, and J. Lord, Phys. Rev. Lett. **77**, 1386 (1996).

[29] R. S. Hayano, Y. J. Uemura, J. Imazato, N. Nishida, T. Yamazaki, and R. Kubo, Phys. Rev. B **20**, 850 (1979).

[30] A. E. Taylor, S. Calder, R. Morrow, H. L. Feng, M. H. Upton, M. D. Lumsden, K. Yamaura, P. M. Woodward, and A. D. Christianson, Phys. Rev. Lett. **118**, 207202 (2017).

[31] We note that the authors of Ref. [8] have extracted an energy barrier to spin reorientation of $\Delta = 204(18)\,\text{K}$ based on a fit of the Arrhenius Law $\omega = \omega_0 \exp(-\Delta/T_f)$ to the peaks in the real part of the AC susceptibility. This fitting procedure has been shown to yield unphysically large energy barriers when applied to spin glasses, as discussed in Refs. [23,45–47], with information about χ'' usually being required to obtain a physically realistic energy barrier.

[32] R. E. Walstedt and L. R. Walker, Phys. Rev. B **9**, 4857 (1974).

[33] R. Khasanov, H. Luetkens, A. Amato, H.-H. Klauss, Z.-A. Ren, J. Yang, W. Lu, and Z.-X. Zhao, Phys. Rev. B **78**, 092506 (2008).

[34] Y. J. Uemura, T. Yamazaki, D. R. Harshman, M. Senba, and E. J. Ansaldo, Phys. Rev. B **31**, 546 (1985).

[35] F. K. K. Kirschner, F. Lang, C. V. Topping, P. J. Baker, F. L. Pratt, S. E. Wright, D. N. Woodruff, S. J. Clarke, and S. J. Blundell, Phys. Rev. B **94**, 134509 (2016).

[36] M. Gerloch, *Magnetism and Ligand Field Analysis* (Cambridge University Press, Cambridge, 1983).

[37] E. König and S. Kremer, *Ligand Field Diagrams* (Plenum, New York, 1977).

[38] A. Georges, L. de' Medici, and J. Mravlje, Annu. Rev. Condens. Matter Phys. **4**, 137 (2013).

[39] J. C. Hempel, J. Chem. Phys. **64**, 4307 (1976).

[40] The parameters Dq, $D\sigma$, and $D\tau$ used in this work correspond to the parameters with the same symbols in Ref. [39].

[41] A. B. P. Lever and B. R. Hollebone, J. Am. Chem. Soc. **94**, 1816 (1972).

[42] J. C. Hempel, R. A. Palmer, and M. C. Yang, J. Chem. Phys. **64**, 4314 (1976).

[43] S. Calder, J. G. Vale, N. A. Bogdanov, X. Liu, C. Donnerer, M. H. Upton, D. Casa, A. H. Said, M. D. Lumsden, Z. Zhao, J.-Q. Yan, D. Mandrus, S. Nishimoto, J. van den Brink, J. P. Hill, D. F. McMorrow, and A. D. Christianson, Nat. Commun. **7**, 11651 (2016).

[44] B. Yuan, J. P. Clancy, A. M. Cook, C. M. Thompson, J. Greedan, G. Cao, B. C. Jeon, T. W. Noh, M. H. Upton, D. Casa, T. Gog, A. Paramekanti, and Y.-J. Kim, Phys. Rev. B **95**, 235114 (2017).

[45] D. Hüser, L. E. Wenger, A. J. van Duyneveldt, and J. A. Mydosh, Phys. Rev. B **27**, 3100 (1983).

[46] D. Huser, A. J. van Duyneveldt, G. J. Nieuwenhuys, and J. A. Mydosh, J. Phys. C **19**, 3697 (1986).

[47] J. Souletie and J. L. Tholence, Phys. Rev. B **32**, 516 (1985).